Affordable Road Obstacle Detection and Active Suspension Control Using Inertial and Motion Sensors

World Electric Vehicle Journal

MDPI

Article

Affordable Road Obstacle Detection and Active Suspension Control Using Inertial and Motion Sensors

Andrew Valdivieso-Soto [1], Gennaro Sorrentino [2,3], Giulia Moscone [2,3], Renato Galluzzi [1,*] and Nicola Amati [2,3]

[1] School of Engineering and Sciences, Tecnologico de Monterrey, Mexico City 14380, Mexico; a01658950@tec.mx
[2] Department of Mechanical and Aerospace Engineering, Politecnico di Torino, 10129 Turin, Italy; gennaro.sorrentino@polito.it (G.S.); giulia.moscone@polito.it (G.M.); nicola.amati@polito.it (N.A.)
[3] Center of Automotive Research and Sustainable Mobility, Politecnico di Torino, 10129 Turin, Italy
* Correspondence: renato.galluzzi@tec.mx

Abstract: The electrification trend characterizing the current automotive industry creates opportunities for the implementation of innovative functionalities, enhancing aspects of energy efficiency and vehicle dynamics. Active vehicle suspensions are an important subsystem in this process. To enable proper suspension control, vehicle sensors can be used to measure the system's response and, in some cases, preview the road conditions and the presence of possible obstacles. When assessing the performance of a suspension system, the speed bump crossing represents a challenging maneuver. A suitable trade-off between comfort and road holding must be found through different phases of the profile. The proposed work uses a fixed-gain observer obtained from Kalman filtering to identify road unevenness and adapt the control strategy when the vehicle travels through a bump. To this end, the obstacle is identified through the use of affordable sensors available in high-end vehicles: accelerometers, inertial measurement units, and stroke sensors. The proposed technique is also affordable from the computational point of view, thus enabling its use in common microprocessors tailored for the automotive field. The bump identification technique is validated through experimental data captured in a vehicle demonstrator. Subsequently, numerical results show that the proposed technique is able to enhance comfort while keeping road holding and attenuating the transient after taking the bump.

Keywords: preview control; sky-hook; ground-hook; Kalman filter; active suspensions

Academic Editor: Michael Fowler

Received: 28 February 2025
Revised: 20 March 2025
Accepted: 24 March 2025
Published: 31 March 2025

Citation: Valdivieso-Soto, A.; Sorrentino, G.; Moscone, G.; Galluzzi, R.; Amati, N. Affordable Road Obstacle Detection and Active Suspension Control Using Inertial and Motion Sensors. *World Electr. Veh. J.* **2025**, *16*, 197. https://doi.org/10.3390/wevj16040197

1. Introduction

The world is currently transitioning toward more electric automotive technologies. Although this trend envisages the full electrification of powertrain and chassis subsystems, the evolution is gradual and deployed in steps. As such, many subsystems in the automotive industry have undergone full electrification. Besides the potential advantages in terms of sustainability, electrified solutions—often classified as x-by-wire—bring better modularity, improved control, robustness, and interconnection with the vehicle network [1]. Semi-active and active automotive suspensions are particularly promising electrified subsystems capable of applying forces at the shock absorber level [2]. This feature becomes attractive when addressing the intrinsic trade-off between ride comfort and road holding. Additionally, the new electric vehicle chassis poses more stringent requirements in terms of vertical dynamics due to the increase in the vehicle mass with the inclusion of battery packs and the implementation of automated driving features.

To attain proper dynamic behavior, different control strategies for controllable suspensions have been developed. Focusing on comfort, Karnopp [3] introduced the extremely popular sky-hook control. This method emulates the presence of a damper between the chassis and the sky, thereby attenuating the vibrations experienced in the passenger cabin. A variation of this strategy is the ground-hook control [4], which seeks to lock the wheel to the ground by adding a proper damping term between the hub and a fixed reference, thus enhancing road holding. To the present day, these two techniques represent the most common suspension control approaches in the automotive industry due to their simplicity and well-known features. However, as demonstrated in this work, a significant drawback of these techniques is their inability to adapt to complex road conditions with sudden profile changes, such as obstacles. This limitation is due to the fact that the two strategies are focused on optimizing either comfort or road holding. Since a trade-off among these two features is necessary, situations in which the opposite behavior is needed are penalized. In addition, bandwidth and saturation limitations of suspension actuators worsen the performance of techniques that are intended for linear, ideal conditions.

Consequently, recent efforts in suspension control have concentrated on optimizing control actions to adapt to varying road conditions. Lu et al. [5] designed a gain-adaptive sky-hook Linear Quadratic Regulator (LQR) and tested it on a truck test rig. More advanced approaches include the so-called preview-based techniques, which augment the control system by adding future information from the road profile and the vehicle environment [6]. Wang et al. [7] used a wheel hub preview for an in-wheel drive intelligent vehicle in which the front wheel obtains the elevation of an irregular road, and the rear wheel uses these data as preview information. Göhrle et al. [8] designed a model predictive control (MPC) for active suspension using a camera to preview the road. Among the preview-processing tools, the most common is the Kalman filter. Doumiati et al. [9] proposed an augmented Kalman filter that uses chassis vertical displacement and acceleration together with suspension deflection data. In a further work, they also employed a Q-parametrization approach to simplify filter design and reduce the computational load [10]. Additionally, Yang et al. [11] formulated an augmented Kalman filter to estimate road unevenness for an adaptive MPC used in active suspension systems.

From the authors' experience with vehicle experiments, bump tests are usually the most critical scenario for vehicles with active suspensions. As mentioned earlier, the challenge mainly derives from the device's power limitation and from the well-known conflict between comfort and road holding. Indeed, soft comfort-oriented damping reduces the vehicle body's vertical acceleration amplitudes, but its oscillations dampen very slowly and vertical tire forces show high dynamic variation, with multiple detachments from the ground soon after the first compression phase. The latter phenomenon is critical for safety since tires cannot produce any lateral or longitudinal forces. Hence, the vehicle cannot be handled in emergency scenarios. As bumps are usually used to slow down vehicles before zebra crossings, guaranteeing vehicle controllability is a safety priority. On the other hand, hard handling-oriented suspension tuning is able to prevent excessive wheel vertical oscillations at the cost of passengers' ride comfort due to the very high forces exchanged with the vehicle, which yield elevated acceleration peaks.

The outlined state of the art is rich with possible approaches to overcome road obstacles. However, in the authors' view, the implementation of many of the strategies is limited. Often, solutions demand excessive economic and computational costs due to the required complexity of the methods or the sensors used. In this context, this research work aims to propose (i) an affordable road obstacle detection method by using inertial and motion sensors, and (ii) a simple bump control strategy by synchronizing a sky-hook and ground-hook control strategy on the basis of the estimated bump geometry. The advan-

tages of this approach are the wide availability of those sensors on passenger cars and the computational simplicity of the proposed mixed strategy.

The remainder of this work is organized as follows. Section 2 presents the road profile estimation method and its validation through experimental acquisitions. Section 3 formulates the proposed control strategy and compares it with some benchmark controllers. Section 4 discusses the simulation results and outlines a quantitative evaluation of the proposed control strategy and the benchmarks. Section 5 concludes the manuscript.

2. Road Profile Estimation

This section describes the road profile estimation methodology and its validation by means of real vehicle acquisitions. The primary goal is the geometrical identification of lumped road obstacles, such as bumps. The proposed method is based on the half-car model to include vehicle pitch dynamics. Previous efforts [9–11] focus exclusively on quarter car dynamics, where pitch information is absent. With this proposal, two possible strategies are formulated for road estimation: (i) an augmented Kalman filter and (ii) a fixed-gain observer to further reduce computational effort. Both estimators employ measurements from accelerometers on the four wheels and on the sprung mass corners, together with suspension stroke sensors. The reference vehicle is a D-class SUV to be equipped with active suspensions. Two bump tests are performed over a bump with 50 mm of height and 400 mm of width, with the vehicle traveling at 20 and 25 km/h with a low fail-safe damping setting. This condition represents the most critical safety scenario in terms of road holding.

2.1. Half-Car Dynamics

Before delving into the details of road obstacle estimation, the half-car dynamic model must be described, as the Kalman filter is a model-based approach. The model considers the pitch and vertical degrees of freedom of the sprung mass (chassis). For the two unsprung masses (wheel hubs), only the vertical degree of freedom is accounted for. Model parameters are tuned to account for the full vehicle mass. In the case of the wheel hubs, the parameters of stiffness, damping, and mass denote the full axle, thereby lumping the left and right wheels [12,13]. The half-car model considered is shown in Figure 1, where the degrees of freedom are highlighted with blue arrows and road disturbances are cyan. The model includes active shock absorbers instead of the usual viscous dampers, and their active force convention is highlighted in red.

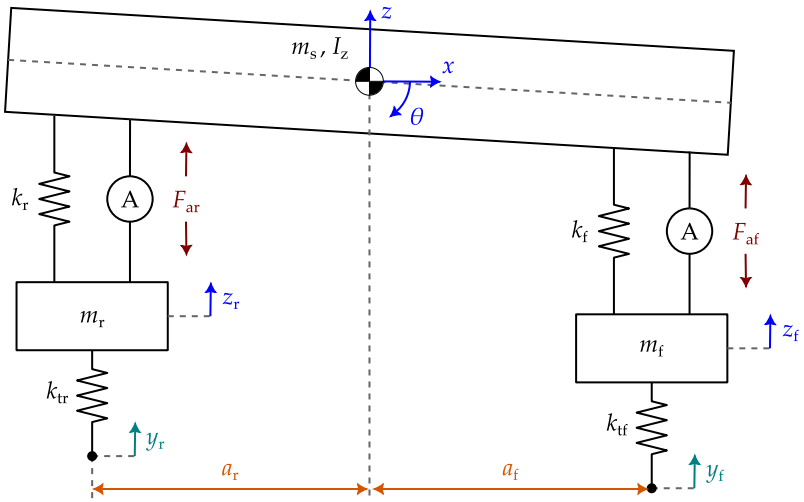

Figure 1. Half-car model of the vehicle describing the vertical degrees of freedom of the chassis (sprung mass) and the two axles (unsprung masses). Chassis rotation denotes pitching motion.

The behavior of this model for the vertical degrees of freedom is affected by input forces F_{af}, F_{ar} and road perturbations z_f, z_r. This model is governed by the following linearized system of equations:

$$m_f \ddot{z}_f = -F_{af} - k_{tf}(z_f - y_f) + k_f(z - z_f - a_f\theta) \quad (1)$$

$$m_r \ddot{z}_r = -F_{ar} - k_{tr}(z_r - y_r) + k_r(z - z_r + a_r\theta) \quad (2)$$

$$m_s \ddot{z} = F_{af} + F_{ar} - k_f(z - z_f - a_f\theta) - k_r(z - z_r + a_r\theta) \quad (3)$$

Equations (1) and (2) express the axles' vertical dynamics, indicated by subscripts f and r for front and rear, respectively. Equation (3) represents the behavior of the chassis. The terms m_f and m_r denote the unsprung masses; m_s the sprung mass, z the vertical displacement of the vehicle body; z_f, z_r the displacements of the axles; k_f, k_r the stiffness of the suspension springs; k_{tf}, k_{tr} the stiffness of the tires; a_f, a_r the two semi-wheelbases; and θ the pitch angle. Expressions (1) to (3) are valid only for small pitch angles θ, following the linearization of the trigonometric functions involving θ.

For the pitch degree of freedom θ, a moment equilibrium around the vehicle body center of gravity is performed, as seen in Equation (4). This expression is also affected by the above-mentioned linearization and the presence of the pitch moment of inertia I_z.

$$I_z \ddot{\theta} = -a_f F_{af} + a_r F_{ar} + a_f k_f(z - z_f - a_f\theta) - a_r k_r(z - z_r + a_r\theta) \quad (4)$$

2.2. Vehicle Setup

The vehicle under study is a D-class SUV with an all-wheel-drive powertrain. Its parameters to reproduce the half-car model are listed in Table 1. It is equipped with accelerometers on three out of four suspension top mounts and four wheel hubs (Bosch PSS2.3X low-g acceleration sensors). Suspension corner deflections are also measured using four stroke sensors (Kyocera AVX 52101 inductive sensors). Additionally, an inertial measurement unit (SBG Ellipse N Inertial Navigation System) installed close to the chassis center of gravity (CoG) allows measuring the vehicle pose; for the purposes of this research, the pitch angle and pitch rate are measured. This setup allows measuring and potentially estimating all the vehicle degrees of freedom outlined in Section 2.1. Furthermore, this sensor layout is common and readily available in high-end vehicles with advanced control features, many of them falling in the segment of the test vehicle used. The objective of this setup is to deploy four fully active shock absorbers in the suspension corners, based on the technology described by Galluzzi et al. [14]. The complete vehicle setup is shown in Figure 2.

Table 1. D-class SUV parameters.

Description	Symbol	Value	Unit
Sprung mass	m_s	2087	kg
Unsprung mass	m_f, m_r	110	kg
Front semi-wheelbase	a_f	1.549	m
Rear semi-wheelbase	a_r	1.269	m
Total wheelbase	ℓ	2.818	m
Front spring stiffness	k_f	51	kN/m
Rear spring stiffness	k_r	66.8	kN/m
Front damping coefficient	c_f	360	Ns/m
Rear damping coefficient	c_r	606	Ns/m
Tire stiffness	k_{tf}, k_{tr}	510	kN/m
Pitch inertia	I_z	4101.9	kgm^2

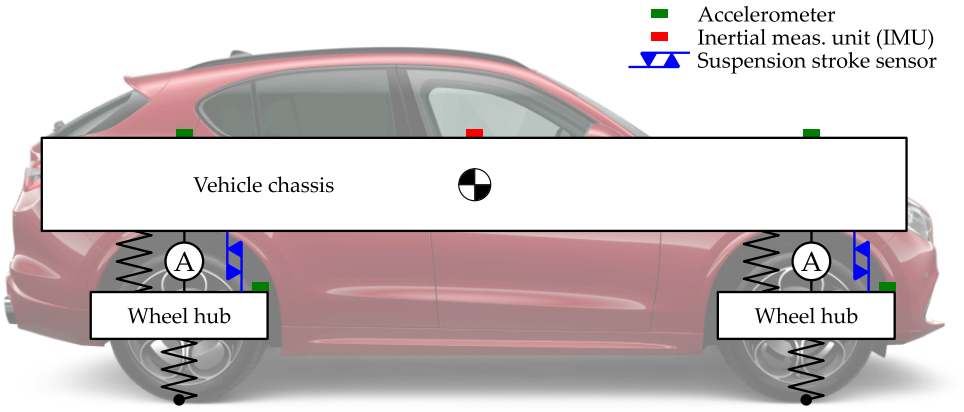

Figure 2. D-class SUV setup equipped with motion sensors and active shock absorbers.

2.3. Bump Test Experiments

This work is based on the analysis of a bump-crossing test. The bump profile exhibits a maximum height of 50 mm and a total width of 400 mm. The test aims at understanding the fail-safe behavior of the vehicle in case of electrical failure of the shock absorber actuators. In this condition, the internal friction of the device represents the only damping contribution of the system: $c_f = 360$ Ns/m for the front axle suspension and $c_r = 606$ Ns/m for the rear one.

The vehicle measurements of interest are reported in Figure 3. In this test, the bump was hit at 0.2 s by the front axle at a real vehicle speed of 18 km/h, as the positive peaks in the acceleration plots and the sudden compression peak in the stroke demonstrate. The rear axle hit the speed bump after 0.5 s, as expected, due to the delay introduced by the wheelbase and the vehicle speed. The sprung mass reached a maximum acceleration of 10 m/s^2 due to the bump hit, while wheel accelerations were more influenced by the rebound phase, reaching peaks around -80 m/s^2. The front suspension traveled a stroke of 6 cm during the first compression phase. The compression end-stop was likely reached in this event, which explains the higher front sprung mass acceleration peak. On the other hand, the more limited rear stroke demonstrates its stiffer architecture. Figure 3a highlights the strong influence of the speed bump scenario over traction. As soon as the obstacle is encountered, the driver releases the throttle pedal and the vehicle's longitudinal speed starts to constantly decrease. The hit affects the rear axle traction more, with the first oscillations at a vehicle speed of ± 2 km/h. Unsprung-mass oscillations are damped faster than the one of the sprung mass thanks to the viscous action of the wheel. Conversely, the sprung mass is strongly affected by the undamped pitch motion due to very low suspension damping. However, the estimated pitch angles confirm the validity of adopting a linear half-car model because the values of θ remain in the range of ± 0.02 rad.

2.4. Road Profile Observer

The measurements available from the motion sensors can be used to estimate the road profile. In this case, a model-based approach is adopted through an augmented Kalman filter. This formulation uses an augmented state vector in which the road profiles and the road velocities at each wheel are included in the state matrix:

$$x_{k+1} = A_k x_k + w_k \tag{5}$$

$$z_k = H_k x_k + v_k \tag{6}$$

where

$$x_k = \begin{bmatrix} z & \dot{z} & z_\mathrm{f} & \dot{z}_\mathrm{f} & z_\mathrm{r} & \dot{z}_\mathrm{r} & \theta & \dot{\theta} & y_\mathrm{f} & \dot{y}_\mathrm{f} & y_\mathrm{r} & \dot{y}_\mathrm{r} \end{bmatrix}^\top \tag{7}$$

$$z_k = \begin{bmatrix} z - z_\mathrm{f} & z - z_\mathrm{r} & \ddot{z} & \ddot{z}_\mathrm{f} & \ddot{z}_\mathrm{r} & \dot{\theta} \end{bmatrix}^\top \tag{8}$$

are the state and observation vectors, respectively, w_k and v_k represent the uncertainty vectors on the model and on the measurements respectively, and the subindex k indicates the number of samples. The state matrix A and the observation matrix H are defined in a continuous state-space representation as follows:

$$A = \begin{bmatrix}
0 & 1 & 0 & 0 & 0 & 0 & 0 & 0 & 0 & 0 & 0 & 0 \\
-\frac{k_\mathrm{f}+k_\mathrm{r}}{m_\mathrm{s}} & -\frac{c_\mathrm{f}+c_\mathrm{r}+c_\mathrm{sf}+c_\mathrm{sr}}{m_\mathrm{s}} & \frac{k_\mathrm{f}}{m_\mathrm{s}} & \frac{c_\mathrm{f}}{m_\mathrm{s}} & \frac{k_\mathrm{r}}{m_\mathrm{s}} & \frac{c_\mathrm{r}}{m_\mathrm{s}} & \frac{k_\mathrm{f}a_\mathrm{f}-k_\mathrm{r}a_\mathrm{r}}{m_\mathrm{s}} & \frac{(c_\mathrm{f}+c_\mathrm{sf})a_\mathrm{f}-(c_\mathrm{r}+c_\mathrm{sr})a_\mathrm{r}}{m_\mathrm{s}} & 0 & 0 & 0 & 0 \\
0 & 0 & 0 & 1 & 0 & 0 & 0 & 0 & 0 & 0 & 0 & 0 \\
\frac{k_\mathrm{f}}{m_\mathrm{f}} & \frac{c_\mathrm{f}+c_\mathrm{sf}}{m_\mathrm{f}} & -\frac{k_\mathrm{f}+k_\mathrm{tf}}{m_\mathrm{f}} & -\frac{c_\mathrm{f}}{m_\mathrm{f}} & 0 & 0 & -\frac{k_\mathrm{f}a_\mathrm{f}}{m_\mathrm{f}} & -\frac{(c_\mathrm{f}+c_\mathrm{sr})a_\mathrm{f}}{m_\mathrm{f}} & \frac{k_\mathrm{tf}}{m_\mathrm{f}} & 0 & 0 & 0 \\
0 & 0 & 0 & 0 & 0 & 1 & 0 & 0 & 0 & 0 & 0 & 0 \\
\frac{k_\mathrm{r}}{m_\mathrm{r}} & \frac{c_\mathrm{r}+c_\mathrm{sr}}{m_\mathrm{r}} & 0 & 0 & -\frac{k_\mathrm{r}+k_\mathrm{tr}}{m_\mathrm{r}} & -\frac{c_\mathrm{r}}{m_\mathrm{r}} & \frac{k_\mathrm{r}a_\mathrm{r}}{m_\mathrm{r}} & \frac{(c_\mathrm{r}+c_\mathrm{sr})a_\mathrm{r}}{m_\mathrm{r}} & 0 & 0 & \frac{k_\mathrm{tr}}{m_\mathrm{r}} & 0 \\
0 & 0 & 0 & 0 & 0 & 0 & 0 & 1 & 0 & 0 & 0 & 0 \\
\frac{k_\mathrm{f}a_\mathrm{f}-k_\mathrm{r}a_\mathrm{r}}{I_z} & \frac{(c_\mathrm{f}+c_\mathrm{sf})a_\mathrm{f}-(c_\mathrm{r}+c_\mathrm{sr})a_\mathrm{r}}{I_z} & -\frac{k_\mathrm{f}a_\mathrm{f}}{I_z} & -\frac{c_\mathrm{f}a_\mathrm{f}}{I_z} & \frac{k_\mathrm{r}a_\mathrm{r}}{I_z} & \frac{c_\mathrm{r}a_\mathrm{r}}{I_z} & -\frac{k_\mathrm{f}a_\mathrm{f}^2+k_\mathrm{r}a_\mathrm{r}^2}{I_z} & -\frac{(c_\mathrm{f}+c_\mathrm{sf})a_\mathrm{f}^2+(c_\mathrm{r}+c_\mathrm{sr})a_\mathrm{r}^2}{I_z} & 0 & 0 & 0 & 0 \\
0 & 0 & 0 & 0 & 0 & 0 & 0 & 0 & 0 & 1 & 0 & 0 \\
0 & 0 & 0 & 0 & 0 & 0 & 0 & 0 & 0 & 0 & 0 & 0 \\
0 & 0 & 0 & 0 & 0 & 0 & 0 & 0 & 0 & 0 & 0 & 1 \\
0 & 0 & 0 & 0 & 0 & 0 & 0 & 0 & 0 & 0 & 0 & 0
\end{bmatrix} \tag{9}$$

$$H = \begin{bmatrix}
1 & 0 & -1 & 0 & 0 & 0 & -a_\mathrm{f} & 0 & 0 & 0 & 0 & 0 \\
1 & 0 & 0 & 0 & -1 & 0 & a_\mathrm{r} & 0 & 0 & 0 & 0 & 0 \\
-\frac{k_\mathrm{f}+k_\mathrm{r}}{m_\mathrm{s}} & -\frac{c_\mathrm{f}+c_\mathrm{r}+c_\mathrm{sf}+c_\mathrm{sr}}{m_\mathrm{s}} & \frac{k_\mathrm{f}}{m_\mathrm{s}} & \frac{c_\mathrm{f}}{m_\mathrm{s}} & \frac{k_\mathrm{r}}{m_\mathrm{s}} & \frac{c_\mathrm{r}}{m_\mathrm{s}} & \frac{k_\mathrm{f}a_\mathrm{f}-k_\mathrm{r}a_\mathrm{r}}{m_\mathrm{s}} & \frac{(c_\mathrm{f}+c_\mathrm{sf})a_\mathrm{f}-(c_\mathrm{r}+c_\mathrm{sr})a_\mathrm{r}}{m_\mathrm{s}} & 0 & 0 & 0 & 0 \\
\frac{k_\mathrm{f}}{m_\mathrm{f}} & \frac{c_\mathrm{f}+c_\mathrm{sf}}{m_\mathrm{f}} & -\frac{k_\mathrm{f}+k_\mathrm{tf}}{m_\mathrm{f}} & -\frac{c_\mathrm{f}}{m_\mathrm{f}} & 0 & 0 & -\frac{k_\mathrm{f}a_\mathrm{f}}{m_\mathrm{f}} & -\frac{(c_\mathrm{f}+c_\mathrm{sr})a_\mathrm{f}}{m_\mathrm{f}} & \frac{k_\mathrm{tf}}{m_\mathrm{f}} & 0 & 0 & 0 \\
\frac{k_\mathrm{r}}{m_\mathrm{r}} & \frac{c_\mathrm{r}+c_\mathrm{sr}}{m_\mathrm{r}} & 0 & 0 & -\frac{k_\mathrm{r}+k_\mathrm{tr}}{m_\mathrm{r}} & -\frac{c_\mathrm{r}}{m_\mathrm{r}} & \frac{k_\mathrm{r}a_\mathrm{r}}{m_\mathrm{r}} & \frac{(c_\mathrm{r}+c_\mathrm{sr})a_\mathrm{r}}{m_\mathrm{r}} & 0 & 0 & \frac{k_\mathrm{tr}}{m_\mathrm{r}} & 0 \\
0 & 0 & 0 & 0 & 0 & 0 & 0 & 1 & 0 & 0 & 0 & 0
\end{bmatrix} \tag{10}$$

Matrices A and H are formulated by assuming a sky-hook suspension control. This method uses a damping coefficient $c_{\mathrm{s}i}$ placed between the sprung mass and the reference [3], with the addition of a relative damping coefficient c_i to stabilize the wheel hop:

$$F_\mathrm{a} = -c_{\mathrm{s}i}\dot{z}_{\mathrm{s}i} - c_i(\dot{z}_{\mathrm{s}i} - \dot{z}_i) \tag{11}$$

Here, $i = \mathrm{f}, \mathrm{r}$ refers to the front (f) and rear (r) axles, and $z_{\mathrm{s}i}$ represents the axle sprung mass vertical position. It is worth noting that the sky-hook formulation is used because in a final implementation, the vehicle is expected to use that control law as the default strategy. However, for the purposes of the experimental identification in this paper, this strategy was disabled, and thus, $c_{\mathrm{s}i} = 0$.

Matrices A_k and H_k are obtained following a backward-Euler discretization of their continuous representation at a period T_s. The linear augmented Kalman filter first performs the prediction step:

$$\hat{x}_{k|k-1} = A_k \hat{x}_{k-1|k-1} \tag{12}$$

$$P_{k|k-1} = A_k P_{k-1|k-1} A_k^\top + Q_k \tag{13}$$

where $\hat{x}_{k|k-1}$ is the state prediction vector at time t_k, and Q_k the noise covariance matrix for w_k. A subsequent correction step is performed as shown below:

$$K_k = P_{k|k-1} H_k^\top (H_k P_{k|k-1} H_k^\top + R_k)^{-1} \tag{14}$$

$$\hat{x}_{k|k} = \hat{x}_{k|k-1} + K_k(z_k - H_k \hat{x}_{k|k-1}) \tag{15}$$

$$P_{k|k} = (I - K_k H_k) P_{k|k-1} \tag{16}$$

where $\hat{x}_{k|k}$ is the state estimation vector and R_k is the noise covariance matrix for v_k. For this estimation task, Q_k and R_k are assumed to be constant, diagonal matrice; i.e., no cross correlation between noises is considered. The weights on the main diagonal of R_k were selected to represent the variance of the noise affecting the experimental data, while the weights of Q_k were tuned empirically to yield an estimate with minimal error when compared to the geometric bump profile.

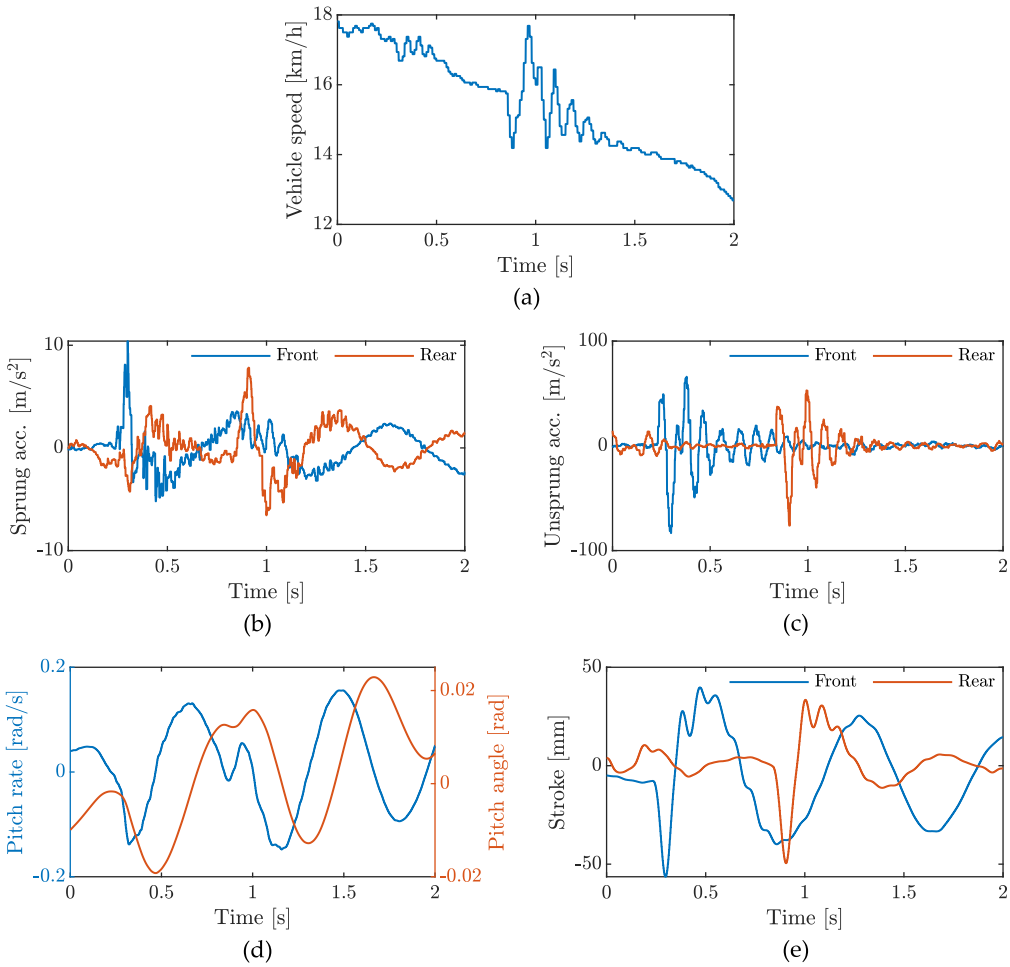

Figure 3. Experimental acquisitions of the speed bump test: (**a**) vehicle speed, (**b**) sprung-mass vertical accelerations, (**c**) unsprung-mass accelerations, (**d**) pitch rate (blue axis) and angle (orange axis), and (**e**) suspension strokes.

$$Q_k = \text{diag}\left(\begin{bmatrix} 10^{-5} & 10^{-5} & 10^{-7} & 10^{-2} & 10^{-9} & 10^{-2} & 10^{-7} & 10^{6} & 1 & 10^{6} & 1 & 10^{6} \end{bmatrix}\right) \tag{17}$$

$$R_k = \text{diag}\left(\begin{bmatrix} 10^{-6} & 10^{-6} & 1 & 16 & 16 & 10^{-4} \end{bmatrix}\right) \tag{18}$$

Once the observer has been tuned and its performance is deemed adequate, a fixed-gain matrix is obtained from the Kalman filter gain K_k. The fixed-gain matrix is obtained by using the value at which the gain K_k converges in the simulation setup. This radically simplifies the calculation of the state updates, thereby avoiding the inversion of a 6×6 matrix when computing K_k. The resulting fixed-gain matrix is given by

$$K_k = \begin{bmatrix} 6.1 \times 10^{-3} & 4.2 \times 10^{-3} & 0 & 0 & 0 & 0 \\ 3.1 \times 10^{-2} & 5.2 \times 10^{-3} & -5 \times 10^{-3} & 0 & 0 & 2.1 \times 10^{-3} \\ -0.12 & 0.16 & 0 & 0 & 0 & 0 \\ -7.9 & 21.5 & 0.31 & 0 & 0 & -0.13 \\ 5.7 \times 10^{-2} & -0.25 & 0 & 0 & 0 & 0 \\ 8.36 & -22.2 & 0.26 & 0 & 0 & -0.11 \\ -4.3 \times 10^{-2} & -1.9 \times 10^{-2} & 0 & 0 & 0 & 0 \\ 3.2 \times 10^{-3} & 5.6 \times 10^{-3} & 1 \times 10^{-3} & 0 & 0 & 1 \\ -0.15 & 0.2 & 1.2 \times 10^{-3} & 0 & 0 & 1.4 \times 10^{-3} \\ -18.1 & 21.9 & 0.28 & 0.1 & 0 & 0.74 \\ 7.6 \times 10^{-2} & -0.3 & 1.1 \times 10^{-3} & 0 & 0 & -1.4 \times 10^{-3} \\ 8.95 & -35.8 & 0.28 & 0 & 9.4 \times 10^{-2} & -0.51 \end{bmatrix} \quad (19)$$

2.5. Experimental Validation

The performance of the estimators is validated using the experimental data collected, as described in Section 2.2. Since this work is focused on using the estimation performed on the front axle to improve the rear suspension control through the preview, the experimental data are used to reconstruct the shape of a bump hitting the front suspensions. This outcome can be used to anticipate when the rear suspension will encounter the same bump, thereby enabling the implementation of the proposed control strategy. Figure 4 shows the results of the experiments performed at two different vehicle speeds i.e., 20 and 25 km/h.

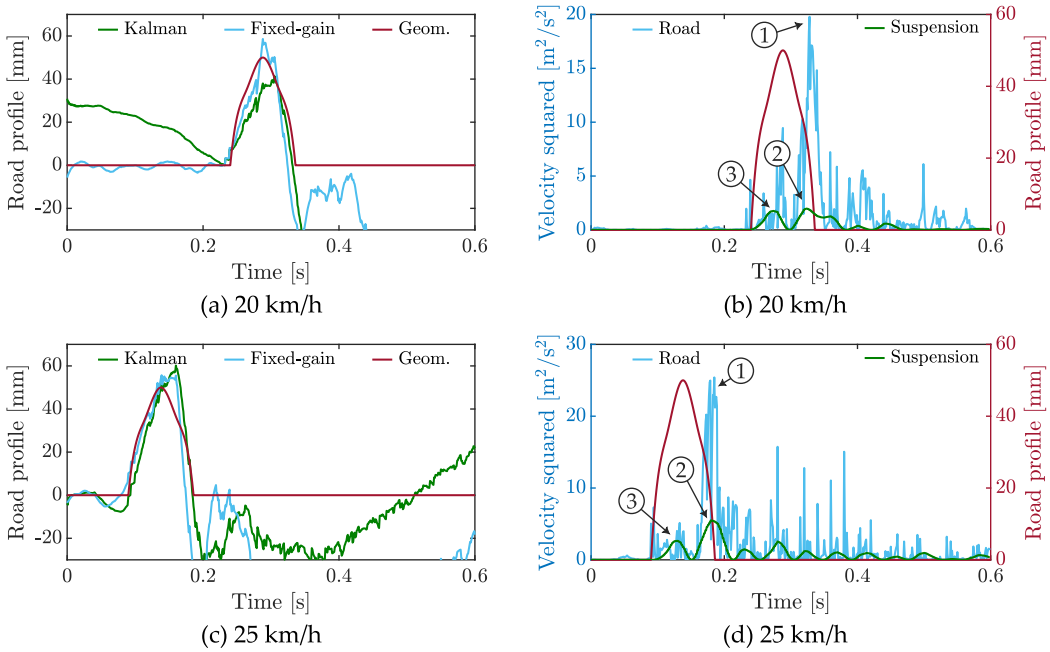

(a) 20 km/h (b) 20 km/h

(c) 25 km/h (d) 25 km/h

Figure 4. Experiments at 20 km/h (**a**,**b**) and 25 km/h (**c**,**d**). Road profile vertical displacement (**a**,**c**); the geometric profile (dark red) is compared to the one estimated with a Kalman filter (green) and a fixed-gain observer (cyan). Bump profile estimation based on the velocity squared (**b**,**d**) from the output of the fixed-gain observer (cyan) and the suspension stroke velocity squared (green). The road profile displacement is shown for reference (dark red, right axis). Points (1) and (2) show maximum peaks of road and suspension velocities squared; point (3) denotes the previous peak of suspension velocity squared.

Kalman filter and fixed-gain estimator results are compared to the geometrical shape of the bump. It is observed that the road profile estimation is performed while taking into account the non-idealities of the tire–ground contact. The shape of the bump changes due to tire deformation. Profile discontinuities are naturally filtered because the tire–ground contact is not punctual; i.e., a contact area is developed. Since this area presents a length along the longitudinal axis, it introduces a phase lead and a smoothing action on the profile perceived by the vehicle. The bump profile exhibits a sudden drop in the second half when the tire loses contact with the road surface. In this case, this contact loss takes place due to the excessive speed at which the bump is overcome.

In the profile estimation, the fixed-gain estimator performs slightly worse than the Kalman filter, overestimating the bump height. However, it reliably identifies the bump's presence and its characteristics. Additionally, the velocity estimation is still reliable. Overall, the fixed-gain estimator represents a considerably more optimized choice because of its lower computational cost compared to the Kalman filter.

The bump position profile is unsuitable for detecting obstacles, as it presents heavy drifting due to the numerical integration of measurement offsets. Hence, the proposed method for bump detection is based on combining the information of road profile velocity and suspension velocity signals. These signal values, obtained by the described observer and by the sensors, are squared, and a threshold value is selected to indicate the presence of a bump. Figure 4b,d show the time behavior of the quantities involved in the bump detection, where the points highlighted by numbers (1) and (2) represent the two peaks in the signals that the strategy aims to identify. Squared velocity thresholds were determined experimentally by analyzing the behavior of these signals in operating conditions of 1.5 m^2/s^2 for the suspension and 15 m^2/s^2 for the road profile. The choice of using the squared value of available physical quantities is due to the necessity of both enhancing the difference between peaks and identifying both bumps and potholes. In the latter case, the control strategy needs to be able to manage both positive and negative peaks in velocity. In addition, the squared velocity value provides insight into the kinetic energy involved during the bump maneuver. Once both thresholds are satisfied in points (1) and (2), the time in which the bump ends, t_{end}, can be captured. This episode can be summarized through the following conditional expression for the ith axle:

$$(\dot{z}_{si,k} - \dot{z}_{i,k})^2 > 1.5\ \text{m}^2/\text{s}^2 \wedge \hat{y}_{i,k}^2 > 15\ \text{m}^2/\text{s}^2 \rightarrow t_{\text{end}} = kT_{\text{s}} \tag{20}$$

To identify the time instant that belongs to the peak height of the bump (t_{max}), the method can recur to the previous peak of suspension velocity squared without applying a threshold:

$$\left(\dot{z}_{si,k-j} - \dot{z}_{i,k-j}\right)^2 > \left(\dot{z}_{si,k-j\pm1} - \dot{z}_{i,k-j\pm1}\right)^2 \forall j \geq 1 \rightarrow t_{\text{max}} = (k-j)T_{\text{s}} \tag{21}$$

This point is highlighted as (3) in Figure 4b,d. The use of a single measurement is possible in the latter case because t_{end} has already been identified through two measurements, so the peak of the bump will be constrained to a previous but close time instant. It is worth noting that the method requires the storage of peak values of the suspension velocity squared, with a buffer length of only one sample.

3. Control Strategies for the Bump Maneuver

The control strategy proposed to overcome a speed bump presents two stages: (i) the reduction in vertical acceleration at the beginning of the bump and (ii) the subsequent fast mitigation of unwanted oscillations related to the wheel hub's transient response. The first stage can benefit from a comfort-oriented strategy like sky-hook control. Its second

counterpart is more related to road holding, where ground-hook control is more adequate. To accomplish this type of control, the road profile is estimated by monitoring the behavior of the front wheel. When a bump is detected, the actuators in the front axle can attempt to compensate for the presence of the obstacle instantaneously. However, the information from the front suspension can be used as a preview for the rear axle.

The framework for the bump-overcoming strategy is illustrated in Figure 5. The vehicle is assumed to travel using a comfort-oriented strategy (sky-hook). When it hits a bump, the profile is filtered by the effect of the tire-ground contact area, as demonstrated in Section 2.5. The filter is a simple moving average based on the contact area length (80 mm), but it is effective in reducing the bump height, smoothing its profile, and anticipating its occurrence. With the assistance of the road profile estimator, the proper timing of the obstacle is obtained. This information is used to properly schedule the vertical dynamics control: sky-hook control is kept to attenuate the first acceleration peaks; subsequently, the strategy is shifted to ground-hook compensation to avoid wheel oscillations. A simple pitch control is also added to the active shock absorber force. The suspension actuator is modeled by a dynamic saturation to bind its power and a low-pass filter to limit its bandwidth.

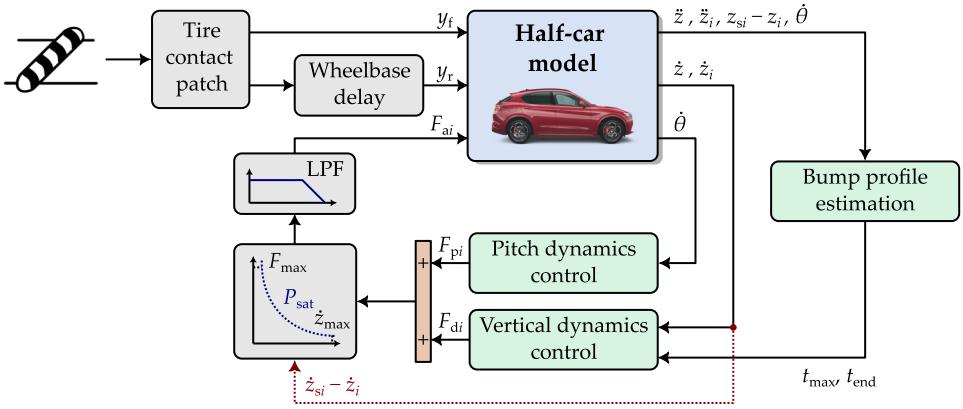

Figure 5. Vehicle simulation setup for the bump maneuver. The subindex $i = \mathrm{f}, \mathrm{r}$ denotes the vehicle axle, front or rear.

To benchmark performance, the proposed predictive control strategy is compared against other strategies; i.e., a full passive system without power limitations, a passively controlled active damper with and without pitch control, and both a sky-hook and a ground-hook coupled to the pitch control module. The comparison is made in terms of weighted sprung mass acceleration, pitch angle and tire forces. The described D-SUV vehicle is used as a numerical evaluation platform with the parameters reported in Table 1.

3.1. Benchmark Control Strategies

To properly evaluate the proposed predictive control strategy, compensation methods based on typical suspension strategies can be simulated. In all of them, the actuator force is given by vertical ($F_{\mathrm{d}i}$) and pitch ($F_{\mathrm{p}i}$) contributions:

$$F_{\mathrm{a}i} = F_{\mathrm{d}i} + F_{\mathrm{p}i} \tag{22}$$

First, a full passive configuration is considered. This setup neglects any compensation of pitch dynamics. Power saturation is also avoided, as in this configuration, the actuator reproduces a fixed damping characteristic without limitations. The passive strategy is governed by

$$F_{\mathrm{d}i} = -c_i(\dot{z}_{\mathrm{s}i} - \dot{z}_i) \tag{23}$$

$$F_{\mathrm{p}i} = 0 \tag{24}$$

where c_i is a fixed viscous damping coefficient, $\dot{z}_{\mathrm{s}i}$ is the axle sprung mass velocity, and the subindex $i = \mathrm{f}, \mathrm{r}$ denotes the front and rear axles. In the following, this configuration will be referred to as *full passive*.

A further modeling step reproduces the full passive strategy with the addition of the motor power limitation as a function of the required force and the suspension velocity. Additionally, actuator dynamics are simplified by means of a first-order low-pass filter with a cut-off frequency of 50 Hz. The considered actuator has a peak power of 3.5 kW, a peak force of 2.5 kN, and a base speed of 1.4 m/s, which represents the speed limit for power derating. This setup is further indicated as *passive control*.

An additional control module specifically targets pitch dynamics with the following laws:

$$F_{\mathrm{pr}} = \frac{a_{\mathrm{f}} c_{\mathrm{p}}}{a_{\mathrm{r}} \ell} \dot{\theta} \tag{25}$$

$$F_{\mathrm{pf}} = -\frac{a_{\mathrm{r}} c_{\mathrm{p}}}{a_{\mathrm{f}} \ell} \dot{\theta} \tag{26}$$

This control simulates a viscous rotational damping c_{p} counteracting excessive pitch motion. The resulting torque is then allocated on the two axles based on their semi-wheelbase. The combination of pitch control and passively controlled active damper will be known as *passive control with pitch*.

Comfort-oriented control is focused on the attenuation of the vertical acceleration of the sprung mass. As mentioned earlier, the comfort-oriented strategy used in this benchmark is the *sky-hook* control (see Equation (11)); hence,

$$F_{\mathrm{d}i} = -c_{\mathrm{s}i}\dot{z}_{\mathrm{s}i} - c_i(\dot{z}_{\mathrm{s}i} - \dot{z}_i) \tag{27}$$

Conversely, handling-oriented control focuses on attenuating the dynamic tire forces. The handling-oriented control used to evaluate the proposed system is the *ground-hook* control. Similarly to the sky-hook control, it emulates a passive damper $c_{\mathrm{g}i}$ connected between the unsprung mass and the reference. The expressions of the ground-hook control technique are reported in Equation (28).

$$F_{\mathrm{d}i} = c_{\mathrm{g}i}\dot{z}_i - c_i(\dot{z}_{\mathrm{s}i} - \dot{z}_i) \tag{28}$$

In the validation tests, both sky-hook and ground-hook strategies are integrated with the pitch motion compensation strategy.

Table 2 summarizes the strategies adopted and their coefficients. Concerning the sky-hook controller, the coefficients were tuned to optimize the vehicle comfort over rough roads, since it represents the usual driving scenario. Ground-hook and pitch control were instead tuned to find the most stable tire force response soon after the bump.

Table 2. Coefficients of the different control strategies.

Control Strategy	c_i [kNs/m]	$c_{\mathrm{s}i}$ [kNs/m]	$c_{\mathrm{g}i}$ [kNs/m]	c_{p} [kNs/rad]
Full passive/passive control	4	0	0	0
Passive control with pitch	4	0	0	86.3
Sky-hook	2	20	0	86.3
Ground-hook	4	0	6	86.3

3.2. Predictive Control Strategy

The *predictive* control aims to provide a simple approach for the bump maneuver by combining the benefits of sky-hook control in reducing sprung mass acceleration peaks at the first impact and ground-hook control in managing wheel hop vibrations when the vehicle is overcoming the bump. The latter aims to ensure the best possible vehicle handling for safety.

The vehicle uses the sky-hook technique by default for comfortable travel on rough roads. As soon as the bump crossing is detected by means of processing the irregularities on the front axle, the control module switches to a ground-hook technique on the front axle until the whole bump maneuver ends on both axles. Damping coefficient transitions between strategies are carried out with a slew rate of 40 kN/m, implying transition times of 50 ms for the coefficients involving the unsprung masses and 500 ms for those related to the sprung mass. This gradual gain scheduling ensures the attenuation of unwanted transients that occur when abrupt changes are requested.

The bump estimation module can also approximate the time at which the bump reaches the maximum height and when it ends. Hence, the rear axle control can schedule, in a preview, the switching from the sky-hook to the ground-hook. The most favorable switching time is when the wheel reaches the maximum bump height because the controller can counteract the wheel's tendency to detach. As before, the control returns to a sky-hook compensation for the normal travel when the acceleration is bounded within ± 0.2 m/s^2 and the suspension has experienced two rebounds.

Figure 6 portrays the predictive control strategy as a function of the bump timing. One can notice the effect of the tire–ground contact area on the geometric bump due to its height reduction and profile lead/lag in time. Notice that in the scenario of encountering multiple bumps, this strategy would hold the suspension in ground-hook control until the bump sequence is overcome by the vehicle.

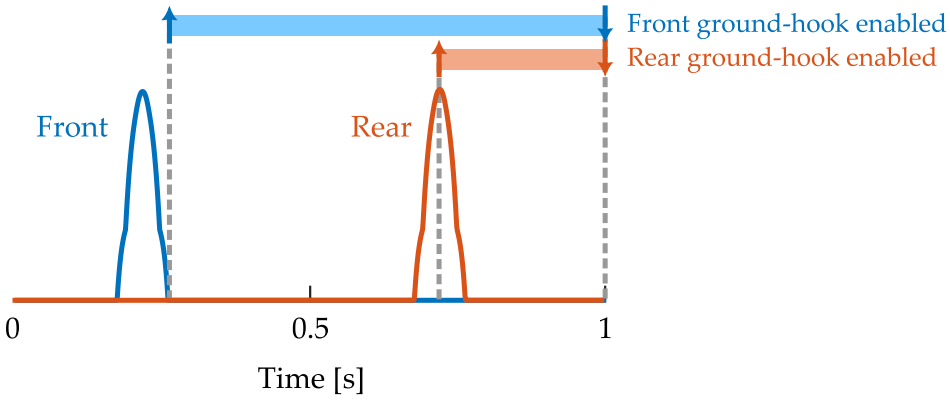

Figure 6. Predictive control strategy as a function of the bump profile estimation.

3.3. Key Performance Indicators for Bump Scenario

Key performance indicators (KPIs) are quantifiable metrics used to assess the quality of the proposed controller with respect to the benchmark strategies. Since the bump scenario is a transient phenomenon, the selected KPIs aim at capturing both the magnitude and the time to settle the computed time histories. In terms of comfort, the root mean square (RMS) value, the maximum absolute value (peak), and the settling time of the sprung mass acceleration are considered. The first one portrays the mean acceleration affecting the vehicle cabin and it directly relates to the specification provided by the ISO 2631 standard [15]. The peak acceleration captures the maximum shock transmitted to the chassis. The settling time is then computed as the time at which the sprung mass acceleration converges to zero, within a tolerance of 0.1 m/s^2, after the bump crossing.

For comfort evaluations, the ISO 2631 standard [15] suggests the use of the acceleration perceived by a human passenger, $\ddot{z}_w$. Equation (29) is the linear adaptation of the ISO 2631 standard with a third-order band-pass filter to obtain $\ddot{z}_w$ from $\ddot{z}$ [16].

$$\frac{\ddot{z}_w(s)}{\ddot{z}(s)} = \frac{80.03s^2 + 989s + 0.02108}{s^3 + 78.92s^2 + 2412s + 5614} \tag{29}$$

To capture the effect of pitch dynamics on comfort, the weighted acceleration computed on both axles will also be reported.

Regarding handling, it is essential to monitor vertical forces, particularly by focusing on two aspects: the number of times the tire loses contact with the ground after a bump—resulting in a complete loss of force or traction capability—and the settling time required to reach the static steady-state force. For this study, the vertical forces at individual corners are analyzed, with the KPIs focusing specifically on the rear corner, as it is the most critical for regaining traction after the bump event, as described in Section 2.3. The vertical force applied to the tire on the ground is defined as negative during compression. In the model, tire detachment is modeled as a force saturation at the corner static weight during the tire rebound phase. Equation (30) expresses the tire forces for both corners.

$$F_{ti} = \frac{k_{ti}}{2}(z_i - y_i) \tag{30}$$

4. Results

For validation purposes, the system described in Section 3 was simulated in a MATLAB/Simulink environment. A linear half-car model was established with the vehicle parameters listed in Table 1. The bump geometry presented in Section 2.2 was used as the road input. Nonlinearities were subsequently added to consider actuator power and wheel force saturation effects. The different control strategies were formulated with basic Simulink blocks. Models were run at a sampling frequency of 1 kHz—well above the bandwidth of interest in a suspension system (100 Hz)—using a Dormand-Prince fixed-step solver.

4.1. Comfort

Figure 7 shows the weighted accelerations of the sprung mass calculated in the CoG of the vehicle. Clearly, the initial oscillations correspond to the front axle passing over the bump, while the rear axle starts to oscillate at 0.68 s. Focusing on Figure 7a, the full passive benchmark reaches the minimum acceleration, about -4 m/s^2 in the rebound phase, since tire detachment results in very high suspension velocities and, consequently, very high damping forces. Actuator power saturation distinctly limits this condition, but subsequent extension oscillations show higher amplitudes. The passive control and the passive control with pitch share the same trend in the sprung mass dynamics. However, while the former is affected by negative peak accelerations during both rebound phases of about -3 m/s^2, the latter shows the highest values of approximately $+3$ m/s^2 at the first compression peaks due to the additional force of the pitch control reacting to the strong variation in its state feedback. Furthermore, pitch control contributes to stopping the low-frequency oscillations starting at 1 s.

Figure 7b reports the actively controlled systems. The sky-hook fails to effectively dampen unsprung mass dynamics, leading to oscillations at the end of the bump. However, it shows the best peak attenuation, reaching a maximum during the rebound phase of about -2 m/s^2. Conversely, the ground-hook has the highest peaks due to the focus on reducing the unsprung mass acceleration with a stiffer suspension tuning, showing a very high peak of $+3.5$ m/s^2 when the rear axle hits the bump. However, it suddenly dampens the unsprung mass dynamics after two complete oscillations, but low-frequency waves are still

present since the ground-hook term excites the vehicle pitch motion. In fact, an unwanted active force on the chassis appears due to the ground-hook term in Equation (28). The predictive control is able to find a compromise between the two. Specifically, it shows lower peaks compared to the ground-hook, but it is also able to effectively dampen unsprung vibrations soon after the bump. The very first acceleration peak is the same as in the sky-hook. The transition toward the ground-hook of the front suspension amplifies the second compression peak, reaching a value of $+2.5$ m/s^2, slightly higher than the ground-hook's response. Instead, the predictive action on the rear axle is able to almost shadow both the sky-hook in the hitting phase and the ground-hook during the rebound. Power saturation affects all the controllers in the first extension peak due to the unavoidable first tire detachment, but only the ground-hook control is affected in the first compression peaks.

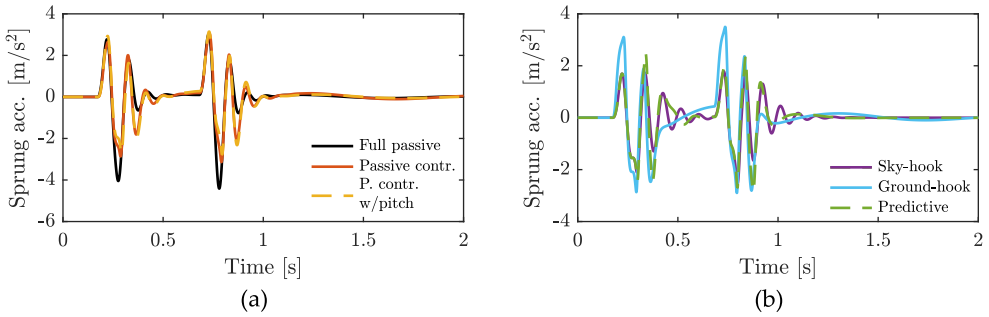

Figure 7. Comparison among the weighted sprung mass accelerations in the CoG: (**a**) fully passive (black), passive with actuator saturation (orange), passive with saturation and active pitch damping control (dashed yellow), (**b**) sky-hook (violet), ground-hook (cyan), predictive (dashed green).

Figure 8 illustrates the pitch angle time histories. The results show a negative value (nose up) when the front wheel passes through the beginning of the bump and a positive value (nose down) when the rear axle travels on it. Focusing on Figure 8a, both the full passive and the passive control are unable to stabilize the pitch motion within 1.8 s after the start of the maneuver. In particular, passive control reaches the highest pitch angle value with $+0.8$ deg due to the power saturation boundaries. The addition of the pitch controller in passive control with pitch effectively attenuates the overall response of the vehicle by reducing the RMS of the pitch angle by 43.75% when compared to the full passive system and keeping its value between ± 0.2 deg.

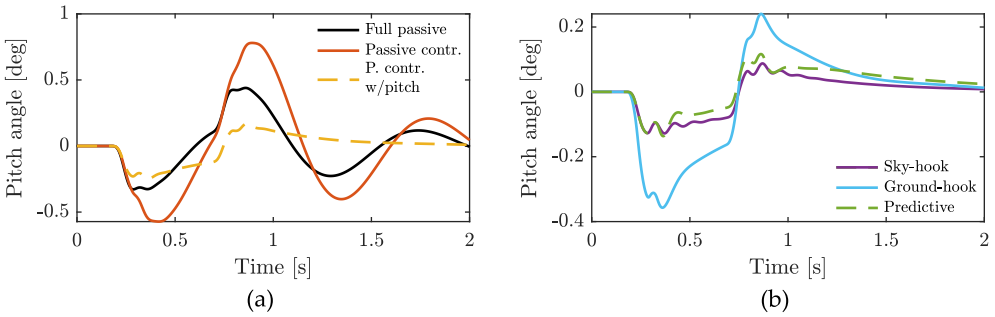

Figure 8. Comparison among the pitch angles: (**a**) full passive (black), passive with actuator saturation (orange), passive with saturation and active pitch damping control (dashed yellow), (**b**) sky-hook (violet), ground-hook (cyan), predictive (dashed green).

As shown in Figure 8b, the sky-hook enhances the pitch behavior because it acts independently on the two axles; it also introduces an additional damping action in pitch dynamics. The pitch angle remains in the interval $[-0.13, +0.09]$ deg. In contrast, ground-hook control reduces the effectiveness of pitch control due to its unintended active effect on the chassis. In the proposed predictive control, when the vehicle crosses the bump

with the front wheel at 0.2 s, the sky-hook on the rear axle contrasts the pitch motion, but when it also hits the bump, the ground-hook simultaneous slightly deteriorates the performance. Overall, the predictive control is still capable of minimizing the pitch angle between $[-0.14, +0.12]$ deg.

4.2. Ride Handling

Figure 9 depicts the time histories of the vertical force on the front corner. In all configurations, the first detachment due to overcoming the bump is unavoidable and the tire force saturates at 5.15 kN. The fully passive control is efficient in damping the tire deflection and is almost unaffected by the rear axle hit, as observed in Figure 9a. Both passive control and passive control with pitch show higher force oscillations soon after the detachments since the power saturation limits the force capability at high suspension speeds. The front tire of the passive control with pitch is also slightly influenced by the bump on the rear axle. From Figure 9b, the unsuitability of the sky-hook in terms of handling is demonstrated by the second detachment of the tire and the very slowly damped vibrations. Instead, the ground-hook outperforms the full passive configuration since it stabilizes the dynamic force of the tire soon after the second tire extension. As expected, the predictive strategy presents a trade-off. A secondary detachment is observed, but it lasts only 0.002 s compared to 0.019 s of the sky-hook and stabilizes the tire dynamics with an additional compression phase. In addition, the results of the predictive control are less affected by the induced pitch motion of the rear axle bump because the initial sky-hook configuration on the rear axle assists pitch control.

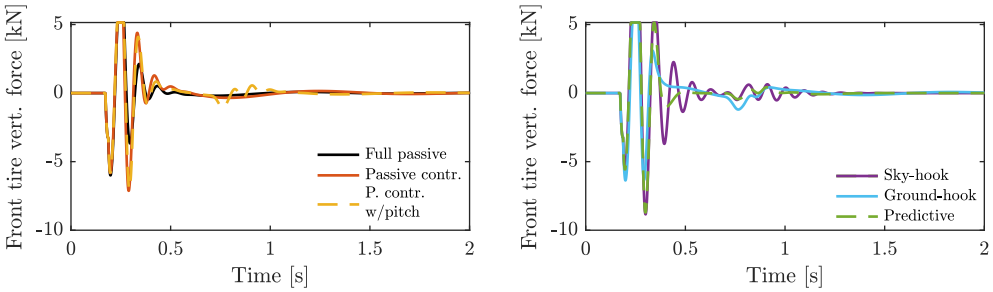

Figure 9. Comparison among the front tire vertical forces: (**a**) full passive (black), passive with actuator saturation (orange), passive with saturation and active pitch damping control (dashed yellow), (**b**) sky-hook (violet), ground-hook (cyan), predictive (dashed green).

Similar considerations are valid for the rear tires, as visible in Figure 10. Tire detachment is denoted by a saturation at 6.17 kN. Obviously, small variations due to the induced pitch motion by the front axle bump arise in the system with active controls.

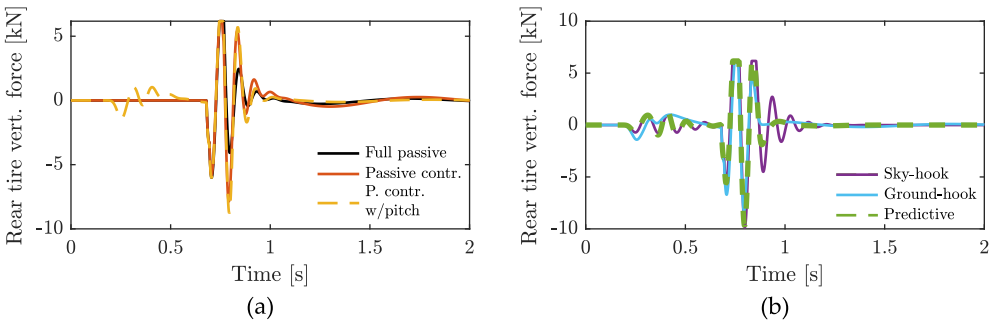

Figure 10. Comparison among the rear tire vertical forces: (**a**) full passive (black), passive with actuator saturation (orange), passive with saturation and active pitch damping control (dashed yellow), (**b**) sky-hook (violet), ground-hook (cyan), predictive (dashed green).

4.3. Discussion

The main numerical results are reported in Table 3 for the comfort metrics and in Table 4 for the handling metrics. The results show that the proposed predictive control improves vehicle comfort compared to the other techniques, except the sky-hook control. However, it is quite predictable since the proposed strategy represents a trade-off between the sky-hook and the ground-hook control. As described in Section 3.3, this manuscript directly deals with a weighted acceleration to consider human sensitivity. In particular, the RMS value of the vertical weighted acceleration in the CoG in the predictive case study is reduced by 21.33% when compared to the full passive system. To also comprehend the influence of pitch dynamics on comfort targets, the weighted acceleration is measured on the two axles; a comparison among control strategies is shown in Figure 11a,b. The rear axle experiences a reduction in the RMS value of 21.21%, while the front axle faces a reduction of 22.60% when the predictive control is compared with the full passive system. As for the peak values, the vertical weighted body accelerations have a reduction of 38.62% on the rear axle and 38.38% on the front axle. The slightly better improvement on the front axle can be justified based on the switching strategy: the front axle is set on a sky-hook strategy for the whole duration of the bump and then switches to a ground-hook strategy after passing it, while the rear axle switches to the ground-hook when it reaches the maximum height of the bump. This means the front axle experiences a comfort-oriented strategy for a longer portion of the maneuver, resulting in a slightly better comfort performance. The other comfort KPI regards the settling time of the vertical acceleration dynamics, whose duration for each considered strategy is shown in Figure 11c. It can be observed that the predictive strategy provides a 3.28% improvement over the full passive system. It is also worth noticing that compared to the other passive strategies, namely the passive control and the passive control with pitch, the improvement of the predictive approach is notably higher, with a decrease of 30.99% and 11.28%, respectively. These two evaluations are important because, in a real vehicle equipped with active suspensions, power saturation affects every control strategy that does not include it in the formulation.

Table 3. Bump-overcoming comfort results.

Control Strategy	RMS Value				Peak Value		Settling Time
	$\ddot{z}_w$ [m/s^2]	$\ddot{z}_{wf}$ [m/s^2]	$\ddot{z}_{wr}$ [m/s^2]	θ [deg]	$\ddot{z}_{wf}$ [m/s^2]	$\ddot{z}_{wr}$ [m/s^2]	$\ddot{z}_w$ [s]
Full passive	0.75	1.15	0.99	0.16	8.99	8.13	1.22
Passive control	0.66	1.01	0.88	0.29	6.36	5.97	1.71
Passive control with pitch	0.65	0.99	0.86	0.09	5.71	5.30	1.33
Sky-hook	0.51	0.74	0.67	0.05	4.18	4.40	1.12
Ground-hook	0.76	1.15	0.99	0.12	6.63	5.91	1.43
Predictive	0.59	0.89	0.78	0.05	5.54	4.99	1.18

Table 4. Bump-overcoming handling results.

Control Strategy	RMS Value		No. of Detachments		Settling Time
	F_{tf} [kN]	F_{tr} [kN]	F_{tf} [–]	F_{tr} [–]	F_{tr} [s]
Full passive	0.88	0.92	1	1	1.81
Passive control	1.05	1.14	1	1	2.30
Passive control with pitch	1.06	1.23	1	1	1.45
Sky-hook	1.30	1.44	2	2	1.12
Ground-hook	1.04	1.19	1	1	1.43
Predictive	1.20	1.34	2	2	1.03

In terms of handling, the first KPI counts the number of detachments to which tires are subjected. The first detachment, as soon as the bump peak is passed, is always inevitable. After that, the more road-holding-oriented strategies manage to avoid the second detachment, while the sky-hook strategy and the predictive one present a second detachment instant, as summarized in Figure 12a. However, the settling time of the rear tire force oscillations is significantly shorter in comfort-oriented strategies, as clearly shown in Figure 12b, because the low-frequency sprung mass vibrations are rapidly attenuated. In particular, the proposed predictive strategy achieves the shortest settling time among all the strategies considered, achieving an improvement of 43.09% over the full passive configuration and even of 3.04% over the sky-hook configuration. This is attributed to the combination of sky-hook control and ground-hook control over the same bump maneuver: the first efficiently dampens the sprung mass oscillations, while the second focuses on attenuating the unsprung mass vertical motion. The subsequent use of both control strategies effectively suppresses, in two subsequent time instants, the two principal harmonics of the vehicle vertical dynamics. This results in a vehicle behavior capable of regaining full controllability in the shortest time interval compared to the other strategies studied.

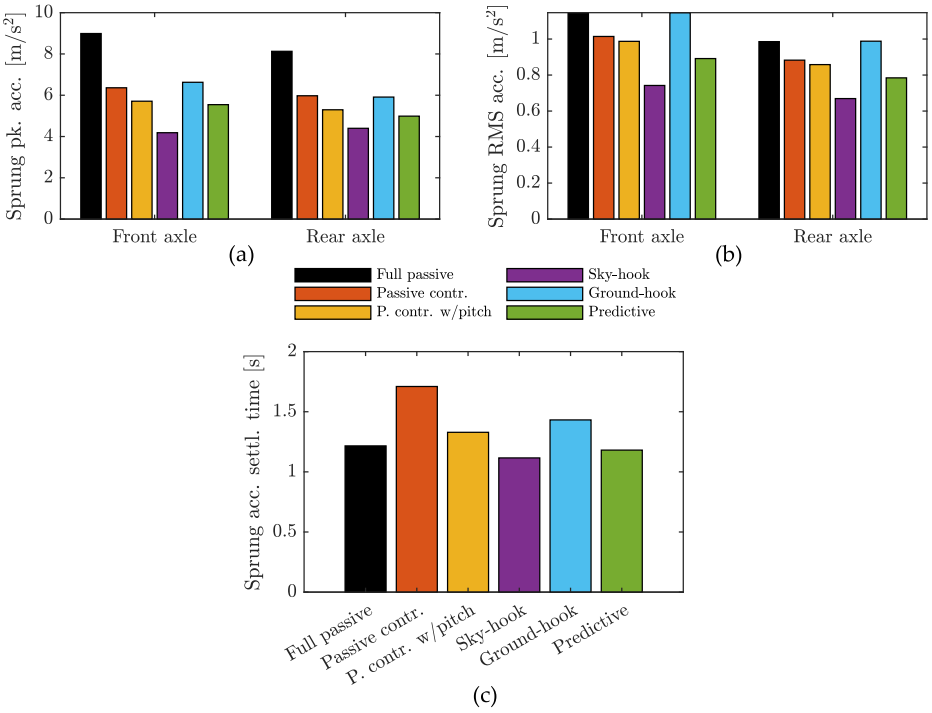

Figure 11. Comparison of comfort key performance indexes in the chassis center of gravity: (**a**) peak absolute value of the weighted sprung mass acceleration, (**b**) RMS of the weighted sprung mass acceleration, and (**c**) settling time of the weighted sprung mass acceleration. Full passive (black), passive with actuator saturation (orange), passive with saturation and active pitch damping control (yellow), (**b**) sky-hook (violet), ground-hook (cyan), predictive (green).

After this analysis, it is clear how the proposed strategy represents a trade-off between the sky-hook and the ground-hook strategies and is able to suitably balance the comfort and the vehicle handling performance to optimize the vehicle response to bumps and potholes. Furthermore, the behavior of the tire force settling time represents an improvement over both pre-existing control strategies, providing a vehicle behavior that compensates for the effects of road obstacles in rapid time.

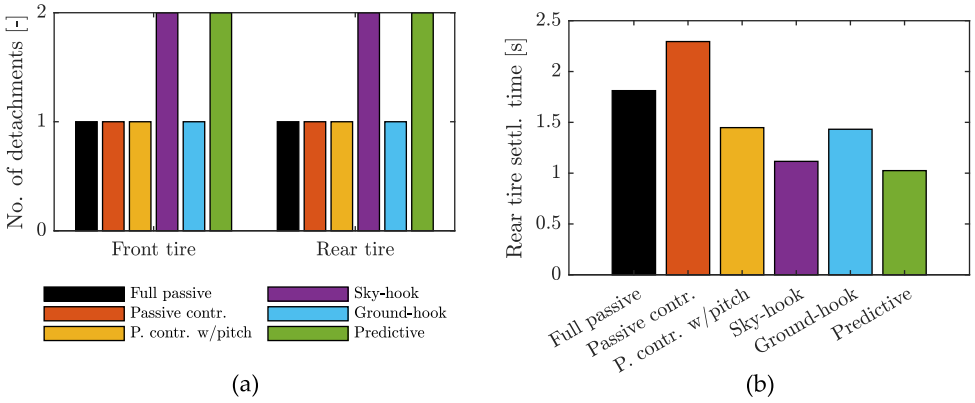

Figure 12. Road-holding KPI comparison: (**a**) number of tire detachments from the ground, (**b**) settling time of the rear tire vertical force. Full passive (black), passive with actuator saturation (orange), passive with saturation and active pitch damping control (yellow), (**b**) sky-hook (violet), ground-hook (cyan), predictive (green).

5. Conclusions

This paper proposed the integration of a road profile reconstruction algorithm and a bump control strategy obtained by switching between a sky-hook and a ground-hook control strategy. The road profile estimation utilizes inertial and motion sensors in the vehicle chassis and suspensions to implement an augmented Kalman filter. The experimental data obtained from a real vehicle passing through a bump are used to evaluate the estimator's correct behavior. Compared to the known profile, the estimated road shows that the system can achieve reliable performance in terms of reconstructing the presence, position, and characteristics of the bumps. The presented approach makes the control strategy affordable, thanks to the use of sensors available in high-end vehicles and the fixed-gain simplification of the filter.

The proposed predictive control approach uses the vehicle's front axle data to obtain information about the bump. The rear axle controller uses the information obtained to enhance the vehicle's performance in terms of both comfort and road holding. This result is obtained by switching between two control strategies: a sky-hook controller is used by default in the vehicle, and it switches to a ground-hook controller to attenuate the wheel-hop at the end of the bump and to improve the tire force behavior and settling time. The described strategy is integrated with a simple pitch control strategy that emulates the presence of a passive viscous damper on the pitch motion.

The proposed strategy was simulated in MATLAB/Simulink using a half-car model. The tests demonstrated that the controller successfully established a trade-off between the comfort and handling performances of the vehicle, obtaining particularly satisfactory results in terms of the settling time of the tire force. The control strategy is hence able to obtain results that are more satisfactory than a simple sky-hook or ground-hook controller and is able to adapt to operational situations without dramatically increasing the complexity or computational cost of the controller.

Future developments of the presented work include the real-time implementation of the proposed strategy in a vehicle equipped with active suspensions.

Author Contributions: Conceptualization, A.V.-S., G.S., G.M., R.G. and N.A.; methodology, A.V.-S., G.S., G.M. and R.G.; validation, G.S. and G.M.; formal analysis, A.V.-S.; investigation, A.V.-S., G.S. and G.M.; data curation, A.V.-S.; writing—original draft preparation, A.V.-S.; writing—review and editing, R.G., G.S. and G.M.; supervision, R.G. and N.A.; funding acquisition, N.A. All authors have read and agreed to the published version of the manuscript.

Funding: This research was funded by the European Commission under grant no. 101138110 (SmartCorners project). Andrew Valdivieso-Soto is funded by Tecnologico de Monterrey, grant no. A01658950, and Consejo Nacional de Humanidades, Ciencias y Tecnologias for scholarship support under the scholarship 1009565.

Data Availability Statement: The original contributions presented in the study are included in the article. Further inquiries can be directed to the corresponding author.

Acknowledgments: This work is supported by the European Commission under the grant no. 101138110 (SmartCorners project). The authors would like to thank the staff at Marelli Ride Dynamics for their valuable support throughout this research activity.

Conflicts of Interest: The authors declare no conflicts of interest.

List of Symbols

The following symbols are used in this manuscript:

m_{f}	Front unsprung mass
k_{f}	Front suspension spring stiffness
k_{tf}	Front tire stiffness
F_{af}	Front axle suspension actuator force
a_{f}	Front axle semi-wheelbase
y_{f}	Front road roughness
c_{f}	Front damping coefficient
F_{df}	Front vertical damping control module actuation force
F_{pf}	Front axle pitch control module actuation force
F_{tf}	Front axle vertical tire force
$\dot{z}_{\mathrm{sf}}$	Front axle sprung mass velocity
c_{g}	Ground-hook damping coefficient
K_k	Kalman gain
x	Longitudinal displacement of sprung mass
w_k	Model uncertainty vector
v_k	Measurement uncertainty vector
Q_k	Model noise covariance matrix
R_k	Measurement noise covariance matrix
z_k	Observation vector
H_k	Observation matrix
P_{sat}	Power saturation
I_{z}	Pitch moment of inertia
m_{r}	Rear unsprung mass
k_{r}	Rear suspension spring stiffness
k_{tr}	Rear tire stiffness
F_{ar}	Rear axle suspension actuator force
a_{r}	Rear axle semi-wheelbase
y_{r}	Rear road roughness
c_{r}	Rear damping coefficient
c_{p}	Rotational damping coefficient
F_{dr}	Rear vertical damping control module actuation force
F_{pr}	Rear axle pitch control module actuation force
F_{tr}	Rear axle vertical tire force
$\dot{z}_{\mathrm{sr}}$	Rear axle sprung mass velocity
m_{s}	Sprung mass
c_{s}	Sky-hook damping coefficient
x_k	State vector
A_k	State matrix
$\hat{x}_{k\|k-1}$	State prediction vector at time t_k

$\hat{x}_{k\|k}$	State estimation vector at time t_k
$P_{k\|k-1}$	State estimate covariance error
$t_{\max}$	Time when the peak bump occurs
t_{end}	Time when the bump ends
ℓ	Total Wheelbase
z	Vertical displacement of sprung mass
$\dot{z}$	Vertical velocity of sprung mass
$\ddot{z}$	Vertical acceleration of sprung mass
z_{r}	Vertical displacement of rear axle unsprung mass
$\dot{z}_{\text{r}}$	Vertical velocity of rear axle unsprung mass
$\ddot{z}_{\text{r}}$	Vertical acceleration of rear axle unsprung mass
z_{f}	Vertical displacement of front axle unsprung mass
$\dot{z}_{\text{f}}$	Vertical velocity of front axle unsprung mass
$\ddot{z}_{\text{f}}$	Vertical acceleration of front axle unsprung mass
θ	Vehicle pitch angle
$\dot{\theta}$	Vehicle pitch rate
$\ddot{z}_{\text{w}}$	Vertical weighted acceleration of sprung mass
$\ddot{z}_{\text{w,f}}$	Vertical weighted acceleration of front axle sprung mass
$\ddot{z}_{\text{w,r}}$	Vertical weighted acceleration of rear axle sprung mass
$\ddot{z}_{\text{w}}$	Weighted vertical acceleration of sprung mass

Acronyms

The following acronyms are used in this manuscript:

CoG	Center of gravity
KPI	Key performance indicator
LQR	Linear Quadratic Regulator
MPC	Model predictive control
PID	Proportional integral derivative
RMS	Root mean square
SUV	Sport utility vehicle

References

1. Genta, G.; Morello, L. *The Automotive Chassis: Volume 1: Components Design*; Mechanical Engineering Series; Springer International Publishing: Cham, Switzerland, 2020. [CrossRef]
2. Savaresi, S.M. (Ed.) *Semi-Active Suspension Control Design for Vehicles*; Elsevier: Amsterdam, The Netherlands, 2010.
3. Karnopp, D.; Crosby, M.J.; Harwood, R.A. Vibration Control Using Semi-Active Force Generators. *J. Eng. Ind.* **1974**, *96*, 619–626. [CrossRef]
4. Valášek, M.; Novák, M.; Šika, Z.; Vaculín, O. Extended Ground-Hook - New Concept of Semi-Active Control of Truck's Suspension. *Veh. Syst. Dyn.* **1997**, *27*, 289–303. [CrossRef]
5. Lu, Y.; Zhen, R.; Liu, Y.; Zhong, J.; Sun, C.; Huang, Y.; Khajepour, A. Practical solution for attenuating industrial heavy vehicle vibration: A new gain-adaptive coordinated suspension control system. *Control Eng. Pract.* **2025**, *154*, 106125. [CrossRef]
6. Theunissen, J.; Tota, A.; Gruber, P.; Dhaens, M.; Sorniotti, A. Preview-based techniques for vehicle suspension control: A state-of-the-art review. *Annu. Rev. Control* **2021**, *51*, 206–235. [CrossRef]
7. Wang, J.; Yang, C.; Liu, S.; Zhang, L.; Fang, J. Vehicle posture wheelbase preview control of in-wheel motors drive intelligent vehicle on potholed road. In *Proceedings of the Institution of Mechanical Engineers, Part D: Journal of Automobile Engineering*; Sage: Los Angeles, CA, USA, 2024; p. 09544070241287247. [CrossRef]
8. Gohrle, C.; Schindler, A.; Wagner, A.; Sawodny, O. Road Profile Estimation and Preview Control For Low-Bandwidth Active Suspension Systems. *IEEE/ASME Trans. Mechatron.* **2015**, *20*, 2299–2310. [CrossRef]
9. Doumiati, M.; Victorino, A.; Charara, A.; Lechner, D. Estimation of road profile for vehicle dynamics motion: Experimental validation. In Proceedings of the 2011 American Control Conference, San Francisco, CA, USA, 29 June–1 July 2011; pp. 5237–5242. [CrossRef]
10. Doumiati, M.; Erhart, S.; Martinez, J.; Sename, O.; Dugard, L. Adaptive control scheme for road profile estimation: Application to vehicle dynamics. *IFAC Proc. Vol.* **2014**, *47*, 8445–8450. [CrossRef]

11. Yang, T.; Li, P.; Li, Q.; Li, Z. Active suspension control strategy for vehicles based on road surface recognition. *Nonlinear Dyn.* **2024**, *112*, 11043–11065. [CrossRef]
12. Kurz, C.; Stangenberg, L.; Gauterin, F. A Generic Approach to Modeling Vehicle Pitch Dynamics on a Vehicle Test Bench. *IEEE Open J. Veh. Technol.* **2023**, *4*, 739–748. [CrossRef]
13. Jazar, R.N. *Vehicle Dynamics: Theory and Applications*, 3rd ed.; Springer: New York, NY, USA, 2009.
14. Galluzzi, R.; Circosta, S.; Amati, N.; Tonoli, A. Rotary regenerative shock absorbers for automotive suspensions. *Mechatronics* **2021**, *77*, 102580.
15. ISO. *Mechanical Vibration and Shock—Evaluation of Human Exposure to Whole-Body Vibration—Part 1: General Requirements*; ISO: Geneva, Switzerland, 1997.
16. Zuo, L.; Zhang, P.S. Energy Harvesting, Ride Comfort, and Road Handling of Regenerative Vehicle Suspensions. *J. Vib. Acoust.* **2013**, *135*, 011002. [CrossRef]